Optimization of GEM detectors for applications in X-ray fluorescence imaging.

Geovane G. A. de Souza[1]*, Hugo Natal da Luz[2], Marco Bregant[1]

1-Instituto de Física, Universidade de São Paulo
Rua do Matão 1371, 05508-090 Cidade Universitária, São Paulo, Brasil
2 - Institute of Experimental and Applied Physics, Czech Technical University in Prague
Husova 5, 110 00 Prague 1, Czech Republic

Abstract

In this work a set of simulations that aim at the optimization of gaseous detectors for applications in X-ray fluorescence imaging in the energy range of 3 – 30 keV is presented. By studying the statistical distribution of the radiation interactions with gases, the energy resolution limits after charge multiplication for 6 keV X-ray photons in Ar/CO_2(70/30) and Kr/CO_2(90/10) were calculated, obtaining energy resolutions of 15.4(4)% and 14.6(2)% respectively. The detector design was also studied to reduce the presence of escape peaks and complement a model to evaluate the inevitable X-ray fluorescence of copper generated by the conductive materials inside the detector.

Keywords: Gas Electron Multiplier, X-ray fluorescence imaging, GEM copper fluorescence

1. Introduction

Micro-pattern gaseous detectors (MPGD) [1, 2, 3, 4] have earned their place in high energy physics and particle physics experiments due to their performance as charge multiplication devices in tracking and particle identifying detectors. MPGDs are a key component in the construction and performance of this type of detectors, but have also reached other applications, showing promising results in the detection of low energy X-ray photons while providing a good position sensitivity, necessary, for example, for cultural heritage studies[5, 6] that can even be complemented with tomography techniques [7]. The main advantage of using such technology is the capability to cover a larger area ($\geq$ 100 cm^2) when compared to solid state detectors, without the need to scan the samples. These techniques have undergone a steady development in the past few years, but there is room to optimize parameters of the detector to obtain more reliable results in this energy range.

In this work a set of simulations is presented focused on the optimization of detectors based on gas electron multipliers (GEM) for X-ray detection. The energy range of interest goes from 3 keV to 30 keV, covering the K or L

*Corresponding author
Email address: geovane.souza@usp.br (Geovane G. A. de Souza[1])

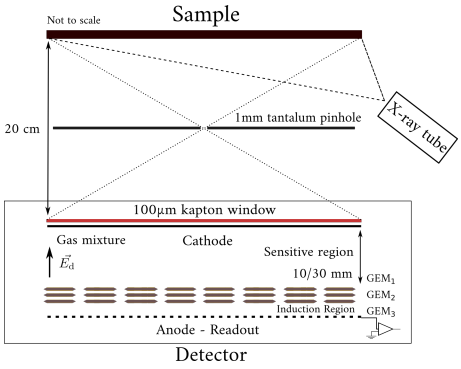

Figure 1: Detector setup used for X-ray fluorescence. Not to scale.

emission lines of most elements. The final aim is the suppression of escape peaks, improving the detection efficiency, and the reduction of the copper fluorescence background generated by the conductive layers of the detector. The simulations were done using Garfield++ libraries[8] and standard C++ code.

In section 2, results regarding the photon conversion efficiency and the energy resolution limits that can be achieved with GEM-based gaseous detectors in the desired energy range are presented. Section 3 shows results related to the photon escape probability and a proposal to reduce the escape peak contribution to the energy spectrum. Since this work is focused in X-ray fluorescence analysis and imaging, a model that describes the extra fluorescence peak generated by the presence of copper in GEM foils was also studied, as described in section 4.

2. Detection efficiency

The X-ray fluorescence imaging setup consists of a triple-GEM foil detector that is operated at atmospheric pressure, using argon and carbon dioxide mixtures at different relative concentrations. The gas flow is set to 6 L/h and the detector is operated with gain close to 2×10^4. The sample is irradiated by a commercial X-ray tube and, by using a pin-hole geometry, the image is projected on the detector as shown in figure 1. After the charge multiplication, the electrons are collected by a segmented strip readout (256 strips for each dimension) interconnected by resistors that allow to reconstruct the position of the interaction by resistive charge division (more details can be found in [9]). There are 20 cm of air and a 100 μm kapton window between the source and the detector, resulting in most of the radiation below 3 keV being absorbed, leading to a limitation on the lowest energy that can be detected. Two different configurations of the detector's absorption region — where the conversion of the photons in electron-ion pairs takes place — were considered, one with 1 cm and the other with 3 cm.

Figure 2 shows the simulated detector efficiency (calculated using the data table from [10]) for three different gas mixtures, Ar/CO_2(70/30), Ne/CO_2(90/10) and Kr/CO_2(90/10), the attenuation due to the air between the sample

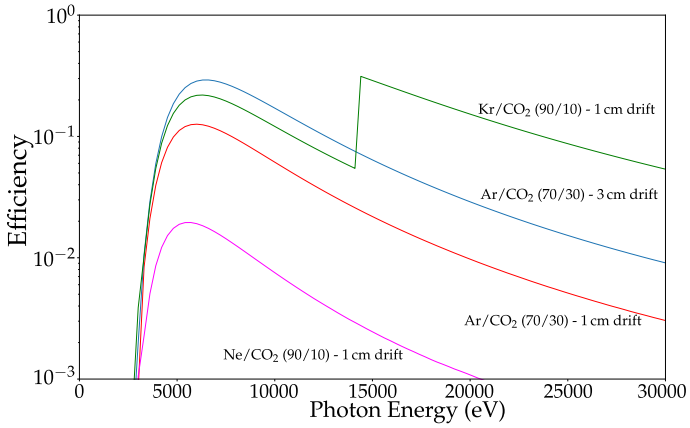

Figure 2: Computed detection efficiency for three different noble gaseous mixtures.

and the detector and due to the kapton window are included in the calculation. Comparing between the different configurations, argon and krypton shows an efficiency of the same order of magnitude up to 14 keV. Above this energy, krypton shows a higher efficiency due to the K absorption edge. Neon has a detection efficiency that is approximately one order of magnitude smaller than the other gasses as expected from its lower atomic number.

To study the statistical fluctuations in the electron-ion pair creation inside the detector and how it influences the energy resolution, the HEED [11] package, which is available inside the Garfield++ program, was used to simulate the interaction of monoenergetic photons inside a gaseous volume filled with Ar/CO_2 or Kr/CO_2 mixtures. The simulation was done for 10^5 photons absorbed by the detector. Figure 3 shows the distribution of the number of primary electrons (Q_p) generated by the 6 keV photon interaction with $Ar/CO_2(70/30)$ and $Kr/CO_2(90/10)$. Both detectors simulated are operating at atmospheric pressure, with dimensions of 10 cm width $\times$ 10 cm depth $\times$ 1 cm height . The number of primary electrons is distributed around a mean value that is proportional to the energy deposited in the drift region. The secondary peak, at lower energy in the plot on the left, is the argon escape peak.

The number of primary electrons generated after the first ionization is described by Poisson processes. However, the distribution is narrower than what is predicted by purely statistical considerations due to the fact that the processes generating the primary cloud are not completely independent from each other. This difference is corrected by the Fano factor [12]. In any case, the more primary electrons are generated, the smaller are the relative fluctuations in this number. The charge amplification mechanism (Townsend avalanche) adds further statistical fluctuations and will generate a final energy distribution which is wider when compared to the primary electrons distribution. Figure 4 shows a simulation of the multiplication factor distribution for a single electron obtained with a single GEM foil detector at different operating voltages. The multiplication factor is defined as the amount of charge collected by the

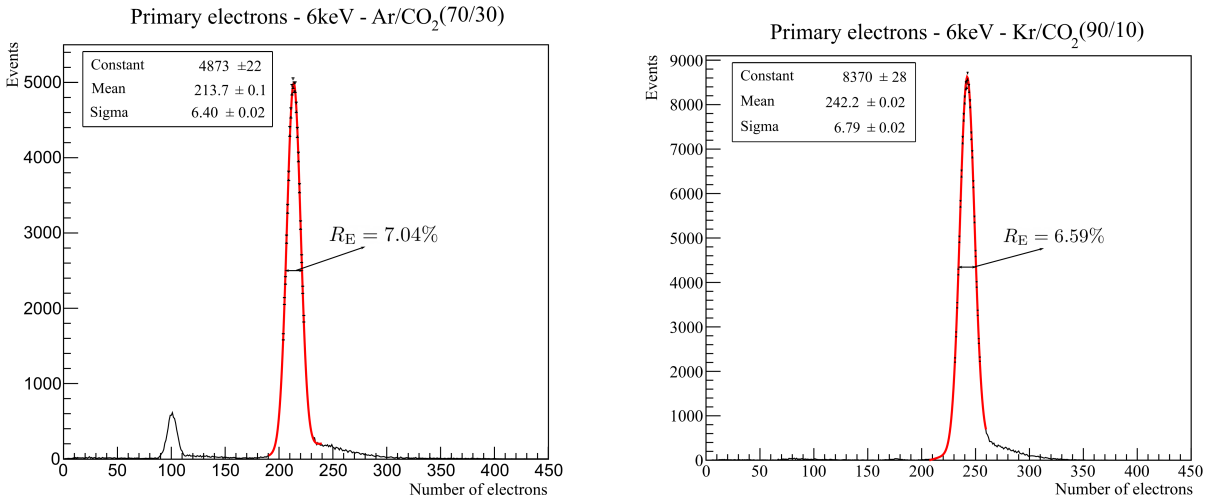

Figure 3: Number of electrons generated in the drift region by monoenergetic photons with 6 keV for argon mixture (left) and krypton mixture (right). The total number of photons interacting was 10^5. The energy resolution is given by the full width at half maximum (FWHM).

readout electronics of the detector (Q_a) divided by the primary charge (Q_p). It corresponds to the effective gain of the detector when applied to the primary electron clouds. The simulated drift field (E_d) was set to 400 V/cm while the induction field (E_i) was kept at 4000 V/cm.

$$G_{\text{eff}} = \frac{Q_a}{Q_p}; \tag{1}$$

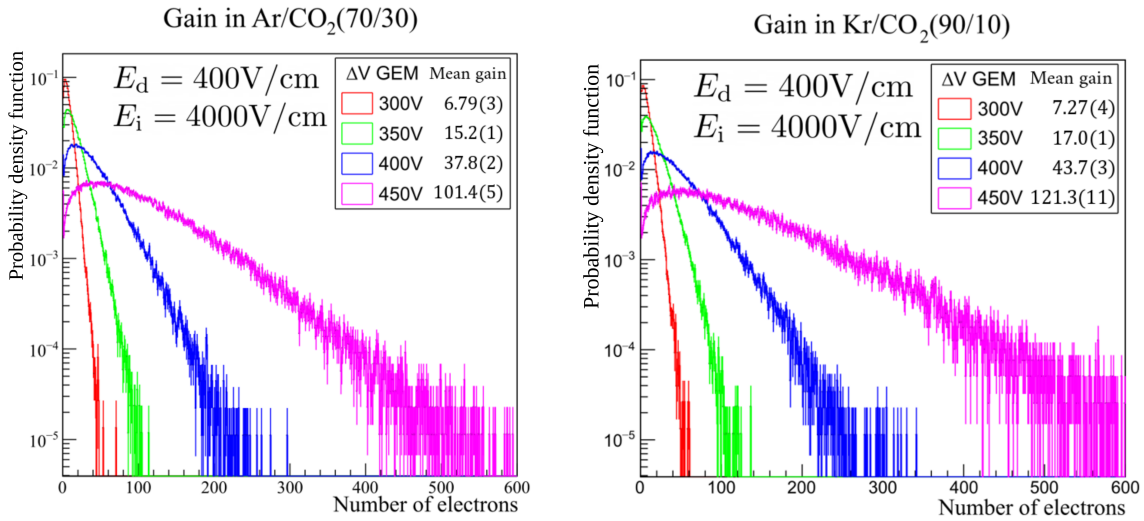

Figure 4: Simulation of the number of electrons produced after the GEM multiplication of a single primary electron.

The Y-axis in figure 4 shows the probability density of each of the occurrences. These probability density distribu-

tions allow to make a Monte-Carlo simulation where for each primary electron from figure 3, a multiplication factor is assigned and a histogram of the final distribution of electrons after a stack of GEMs foils is computed. Figure 5 shows the electron distribution after multiplication, using the gain curve for 350 V. As expected, after the multiplication the energy resolution is degraded due to the statistical process that takes place in the multiplication. The same procedure was made for a stack of two and three GEM foils, however, no considerable difference in the energy resolution could be found, reflecting the smaller statistical fluctuations due to the much larger number of electrons now available. The value obtained is important since it shows the best energy resolution that can be achieved with ideal GEM foils, neglecting other effects such as electronic noise or detector non uniformity. The energy resolution is limited by the amount of primary electron-ion pairs generated by one photon. For 6 keV the value for the energy resolution before charge multiplication in Ar/CO_2 was close to 7% (FWHM), at atmospheric pressure. However, it is mandatory to use a structure such as the GEM foils to increase the signal-to-noise ratio, and after charge multiplication, the value for energy resolution degrades to 15% (FWHM), which may cause uncertainties in the identification of elements with adjacent atomic numbers. The same effect was simulated in $Kr/CO_2(90/10)$ and since the Fano's factor for Krypton and Argon [13, 14] are similar, and also the effective gain achieved [15], the resolution degradation was similar.

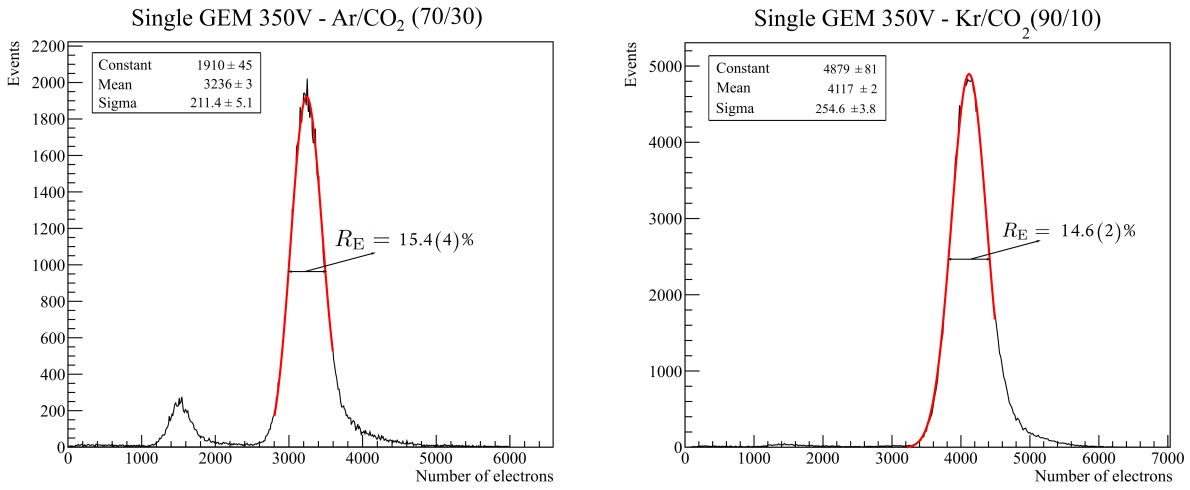

Figure 5: Number of electrons (generated by 6 keV photons) collected at the anode after multiplication by a single GEM foil. The resolution is the FWHM.

3. Photon escape probability

In the energy spectra of the argon-based mixture shown in figures 3 and 5 the escape peak can be clearly seen, with lower intensity and less energy than the main peak. It is generated by events where the energy of the incident photons is not completely deposited inside the detector. When the secondary X-ray photon, produced by the gas de-excitation

escapes the detector without interacting, less energy is deposited in the detector. For argon, the energy of the X-ray photon emitted is 3 keV (a transition between the L and K shells) and for krypton 1.5 keV (the transition between M and L shells — for incident energies below 14 keV). The escape probability for the krypton fluorescence photon is much smaller due to its lower energy. For each characteristic X-ray line in the detected energy spectrum an escape peak is generated with a well known energy defined by the filling gas. This poses a challenge when trying to identify elements by spectral analysis, due to the overlapping of the escape peaks with the fluorescence lines emitted by the sample under study. To better understand such effects, one can simulate the probability of a photon escaping as a function of the height of the drift gap and the type of gas used inside the detector.

From the Lambert-Beer equation, which describes the attenuation of the intensity of photons in matter, the probability of transmission through a certain thickness of material is determined by:

$$P(x) = e^{-\frac{x}{\lambda}}, \tag{2}$$

where x is the length traveled by the photon inside the medium and λ is the attenuation length for a given energy in the same medium. The two different detector configurations mentioned above were considered, the first one with a 1 cm absorption region and the second with 3 cm, both square with an active area of 100 cm^2, operating with Ar/CO_2(70/30) at atmospheric pressure. To calculate the escape probability at each point of the entire volume, photons were generated isotropically and the total travel length for each one was calculated analytically.

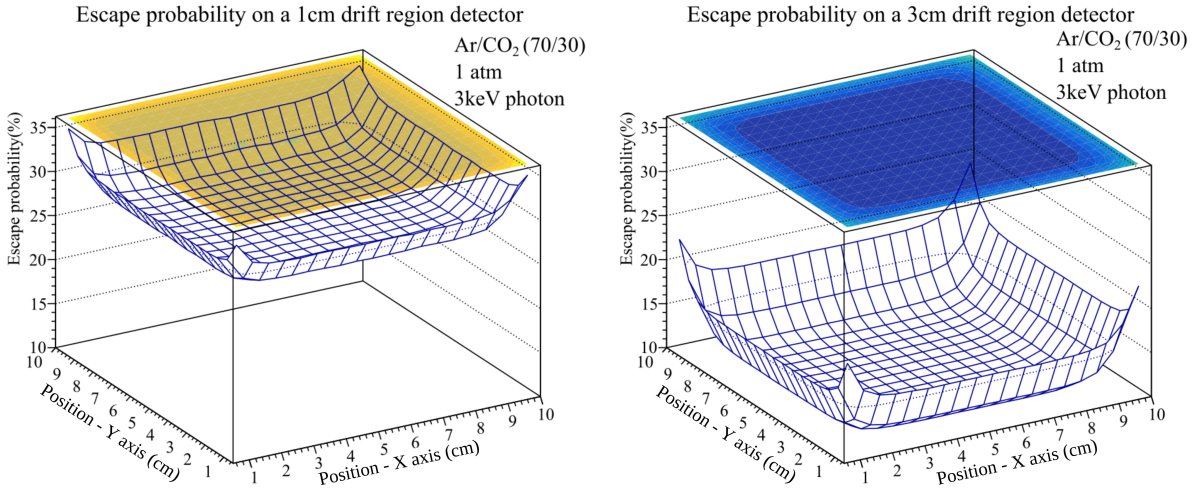

Figure 6: Escape probability for two different geometries. For the drift region with 3 cm the escape probability is substantially lower.

Figure 6 shows the escape probability for a photon of 3 keV, argon's K_α fluorescence energy, for different positions in the detector. One can notice how much the escape probability drops just by increasing the drift region by 2 cm.

Also, by increasing the argon concentration in the mixture the escape probability for the whole detector decreases, as figure 7 shows. The result shown in figure 7 is due to the fact that the interaction cross-section for photons of 3 keV is higher in argon than in carbon dioxide [16]. Increasing the concentration of argon however, affects other parameters such as gain and operation stability .

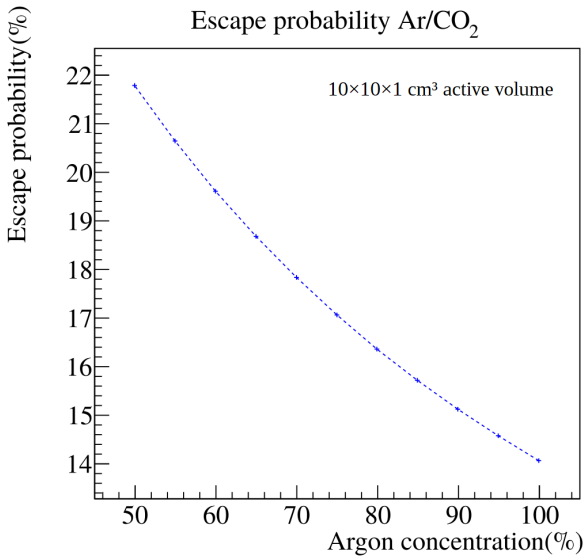

Figure 7: Escape probability as a function of the argon concentration in the gaseous mixture with carbon dioxide.

If there is a necessity to work with shorter drift lengths, it is necessary to use gasses with a larger atomic number, increasing the X-ray absorption cross section and, depending on the incident energies, also decreasing the energy of the secondary photons. Krypton only emits the K_α line if it is ionized by radiation with energy higher than 14 keV. For lower energies, the L_α transition emits a photon with 1.59 keV[17]. Since this energy is lower, the probability to absorb these photons is higher, and the complete energy of the event is deposited in the gas in most of the interactions. Figure 8 shows that the probability of a secondary photon escaping the detector is much lower than for argon.

4. Copper background in the energy spectra

One of the challenges regarding the detection of fluorescence X-ray photons with an imaging system based on GEMs is the background added to the energy spectrum generated by the copper electrodes for X-ray energies above 8 keV. A part of the radiation which does not interact in the drift region may hit the copper cladding of the GEM foil or the readout electrode, generating fluorescence X-rays that can enter the absorption region. The characteristic K-shell of copper has an energy of 8.05 keV [17], inconveniently close to the efficiency peak of our system, as shown before in figure 2. As calculated previously, the energy resolution limit for our detector is around 15% at this energy

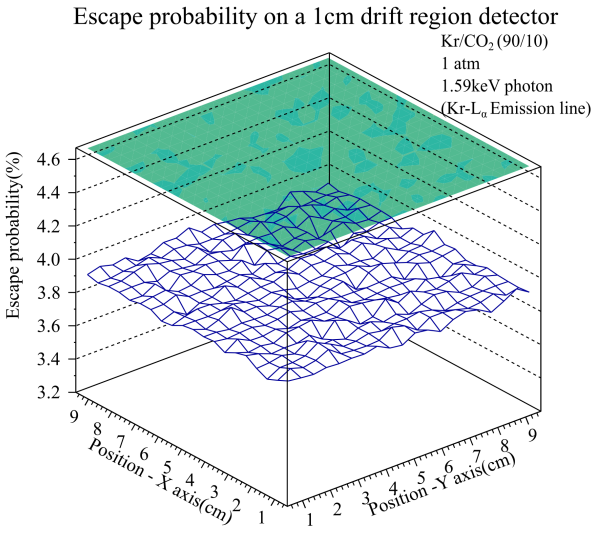

Figure 8: Escape probability for a 1 cm drift region gap. The escape probability is one order of magnitude lower than the one with argon. There are also border effects similar to those seen for argon, but they happen much closer to the boundaries of the detector at distances neglected in this calculation.

range and the presence of this peak may jeopardize the identification of elements. Figure 9 shows how the process happens.

To estimate the contribution of the copper background to the energy spectrum, a model that is widely used in XRF spectroscopy [18, 19] was studied and complemented. The simulation was made taking into account the amount of fluorescence photons created in each electrode of the detector, that is, the top and bottom electrodes of each GEM foil and the readout plane. The final result is the sum of all these contributions.

The probability of detecting a photon dI_k, that comes from the fluorescence K_α of copper and is emitted by the infinitesimally thin layer dy of the top copper cladding of the first GEM foil, can be obtained as following:

$$dI_k(\nu_i, \nu_f) \propto \frac{d\Omega}{4\pi}\omega_k \frac{1}{\lambda_k(\nu_i)} \exp\left(-\frac{y}{\lambda_{Cu}(\nu_i)}\right)\exp\left(-\frac{z}{\lambda_{Cu}(\nu_f)}\right)dy \tag{3}$$

where the variables are depicted in fig. 9.

The first exponential term gives the intensity of the beam (with energy ν_i) that reaches the infinitesimal layer of copper (dy) after traveling a copper length of y. The second exponential is the attenuation of the fluorescence photons (with energy ν_f) that are generated inside this same infinitesimal layer and that pass through a total length of z inside the copper. The term $\frac{1}{\lambda_k(\nu_i)}$ is related to the differential probability of photon fluorescence emission and takes into account only interactions which generated K-shell vacancies. In a first approximation, at these energies, the difference between the attenuation length using all the electronic shells or only the K-shell is small [20] and can be neglected,

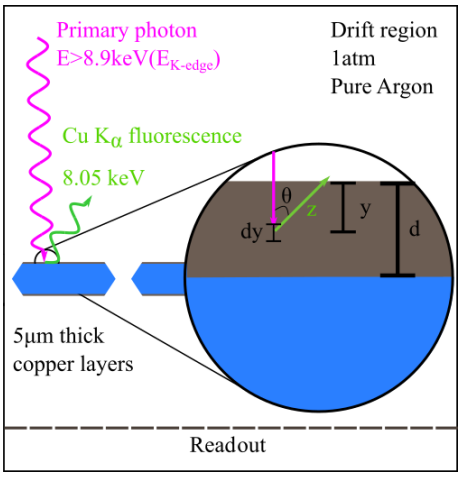

Figure 9: Schematics of the paths traveled by the primaries and fluorescence photons.

that is, $\frac{1}{\lambda_k(\nu_i)} \approx \frac{1}{\lambda_{Cu}(\nu_i)}$. The term $\frac{d\Omega}{4\pi}$ will give the solid angle covered by the active area of the detector (the drift region) and ω_k is the fluorescence yield, that is, the probability of the K-shell vacancy be filled through radiative processes. The value used was 0.433, obtained from [21].

To obtain the probability of fluorescence photons being detected ($d\bar{I}_k$), two extra terms need to be added into this equation. The first one, $\gamma(\nu_i)$ is the term related with the attenuation by the different materials with which the photon beam may interact before going through the copper layer (that is, the air column between the source and the detector and the window and drift region transmission) and is energy dependent. The second is the probability of detection of the fluorescence photons by the drift region, considering that they are not absorbed by any other material until they reach the absorption region. Taking into account the angle emission, one can write $z = \frac{y}{\cos(\theta)}$ (also applying it to the path inside the drift region), leading to the following:

$$d\bar{I}_k(\nu_i, \nu_f) = \frac{d\Omega\gamma(\nu_i)\omega_k}{4\pi\lambda_{Cu}(\nu_i)} \exp\left[-\left(\frac{y}{\lambda_{Cu}(\nu_i)} + \frac{y}{\lambda_{Cu}(\nu_f)\cos(\theta)}\right)\right]\left(1 - \exp\left[\frac{-D}{\lambda_{Ar}(\nu_f)\cos(\theta)}\right]\right)dy \tag{4}$$

where D is the drift region thickness and $\lambda_{Ar}(\nu_f)$ is the argon attenuation length. The total intensity for the first copper layer of the first GEM foil can be obtained by integrating over the thickness of the copper cladding (d) and the solid angle:

$$\bar{I}_k(\nu_i, \nu_f) = \frac{\gamma(\nu_i)\omega_k}{4\pi\lambda_{Cu}(\nu_i)} \int_0^{2\pi} d\phi \int_0^{\frac{\pi}{2}} d\theta \sin(\theta) \int_0^{d} dy \exp\left[-\left(\frac{1}{\lambda_{Cu}(\nu_i)} + \frac{1}{\lambda_{Cu}(\nu_f)\cos(\theta)}\right)y\right] \left(1 - \exp\left[\frac{-D}{\lambda_{Ar}(\nu_f)\cos(\theta)}\right]\right) \tag{5}$$

Integrating over d and ϕ, and re-writing $\frac{1}{\lambda_{Cu}(\nu_i)}$, $\frac{1}{\lambda_{Cu}(\nu_f)}$ and $\frac{1}{\lambda_{Ar}(\nu_f)}$ as a, b and c respectively the following equation is obtained:

$$\bar{I}_k(\nu_i,\nu_f) = \frac{\gamma(\nu_i)\omega_k}{2}\int_0^{\frac{\pi}{2}} d\theta \sin(\theta)\frac{a}{a+b\cos(\theta)}\left(1-\exp\left[-\left(a+\frac{b}{\cos(\theta)}\right)d\right]\right)\left(1-\exp\left[\left(\frac{-Dc}{\cos(\theta)}\right)\right]\right) \tag{6}$$

This integral can be solved numerically however, some additional boundary conditions were added to the problem. The first one is that the X-ray source is considered to be far enough from the detector window to consider all the photons entering the drift region perpendicularly to the detector plane. The detector is considered to have an infinite area, and the GEM foils and readout strips are considered continuous electrodes, neglecting the GEM holes and the strip structure at the readout plane. These conditions were assumed in order to simplify the problem and it is expected that they would change the problem just by a small scale factor. The values for the attenuation length used were obtained using the tabulated values [10, 16]. To calculate the contribution of the other copper electrodes, more attenuation terms are taken into account.

Figure 10 shows the fluorescence absorption contribution from three different layers inside a triple-GEM detector, the first and second copper electrodes from the stack and the readout plane. The contributions, shown as a function of the fluorescence emission angle, were calculated using equation 4 by applying the additional terms in the case of a triple stack.

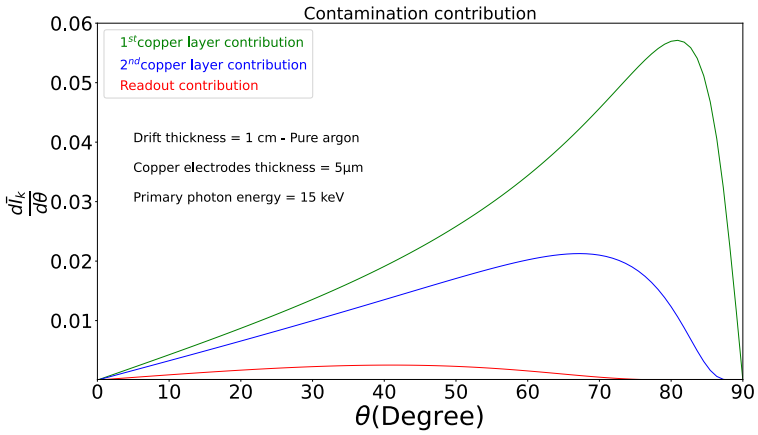

Figure 10: Copper fluorescence generated inside the detector by different layers as a function of the emission angle.

It is clear that the contribution of fluorescence photons detected that were generated in layers which are deeper inside the detector are smaller. To estimate the total contribution for a specific detector setup one needs to add additional attenuation terms for each subsequent electrode, and integrate and sum each one of their contributions. Figure 11 shows the total copper fluorescence detected for two different systems. The one on the left side has a drift region with 1 cm, while the second one, on the right side, has a drift with 3 cm. Both detectors have three GEM

foils and a readout covered by copper and each one of these electrodes is 5 µm thick. The gap between GEM foils is considered 1.5 mm and between the last GEM foil and the readout plane is 1 mm. The value for γ in the first layer calculation was kept equal to the transmission probability in the drift region and for the inner copper layers, the terms related to the transmission in other components were added. The fluorescence photons from these inner layers will also be attenuated by the components that are above them (for example, a fluorescence photon which is generated in the top layer of the second GEM foil will have a specific probability of interacting anywhere in the transfer region and the first GEM foil of the stack).

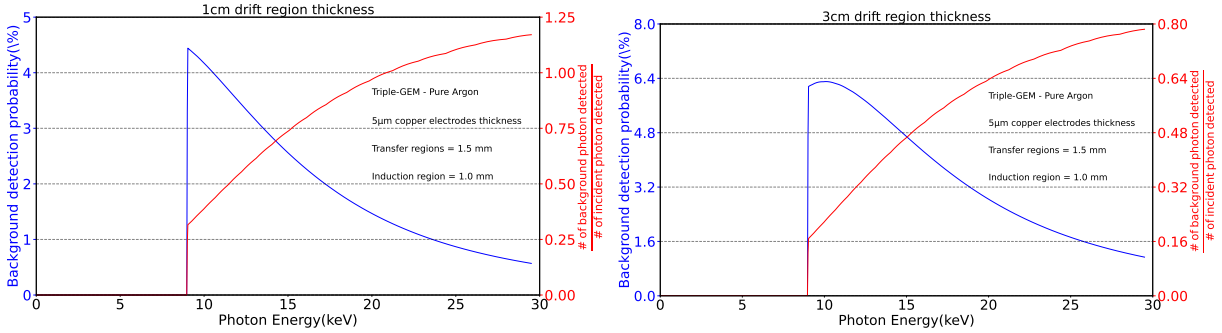

Figure 11: Copper fluorescence detection probability (blue) and fluorescence detection fraction (red) for 1 cm and 3 cm drift thickness.

One can see that the probability of a fluorescence from copper (blue curve) has its maximum just above the K-shell absorption edge and then it drops. This happens mainly due to the increase of the attenuation length for higher energy primary photons, while the attenuation length for the copper K_α photons remains constant. In red (secondary Y-axis) it is possible to see the fraction of fluorescence photons detected with respect to the number of primary photons. The ideal is to minimize this ratio, increasing the number of primary photons which are detected, thus, the detector with thicker drift region shows more advantages. It is simple to understand that this pollution worsens the position resolution of the detector (these photons are going to create a flat background in the images, decreasing the contrast over the whole active area) and of course, will generate a extra peak at 8.05 keV plus the correspondent argon escape peak at 5 keV.

Different groups are working in methods to suppress the fluorescence of copper in GEM-based detectors. One idea is to remove most of the copper conductive layer and to use only the adhesive which glues the copper to the dielectric as a conductor [22, 23]. This layer has chromium in its composition, which can also produce a fluorescence, however, it is much thinner and should not affect the energy spectrum as much as the standard conductive layer made of copper. Another alternative is to use a different cladding for the GEM foils, replacing the copper by another metal with a smaller atomic number. Aluminum may be one of the candidates, with X-ray fluorescence at 1.48 keV which will not affect the energy spectrum in the region of interest [24]. Figure 12 shows the total fluorescence calculated for

a aluminum-clad triple-GEM detector operating with a copper readout.

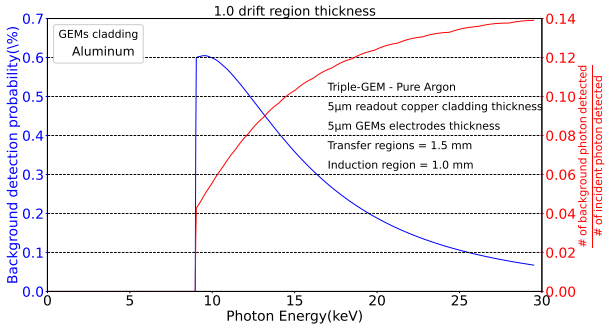

Figure 12: Copper fluorescence detection probability for a triple-GEM detector using aluminum cladding and copper readout.

The relative dimensions were kept the same as the ones for the previous configurations and there is no possibility of fluorescence of aluminum, because only photons with energies well above the Al fluorescence threshold are able to reach the drift region. One can see that the probability of generating a fluorescence photon of copper is small in the system using aluminum GEMs because only the copper present in the readout is contributing for this background and also the ratio between fluorescence photons and primary photons detected is smaller in this system. Although this is a promising result, the etching of aluminum foils may be more difficult and this electrode may show oxidation problems in a shorter time than the copper one.

5. Conclusion and outlook

Gaseous detectors have shown their importance in high energy physics experiments and they also may be used for other applications such as XRF, PIXE and X-ray diffraction if the correct parameters and detector assembly are chosen. The main advantage of using such detectors is connected to the large sensitive areas that are possible to manufacture, without prohibitively increasing their price and that can dramatically reduce the scanning time of large samples. For applications such as XRF it was shown that the spectral analysis may present some challenges due to the limitations in energy resolution which does not allow distinguishing neighboring elements in the periodic table.

The detection efficiency can achieve larger values and the escape peak interference may be suppressed at a point that it stops influencing the final spectrum by increasing the depth of the drift region or by changing the gas according to the specific application. Everything will depend on the needs of the experiment and availability of material.

Regarding the copper fluorescence background in the energy spectrum, it was possible to evaluate the probability to detect undesired fluorescence photons. Showing that detectors with larger drift regions or without copper in its composition will be more robust against the contamination of the energy spectra with fluorescence X-rays from the copper surface of the GEM foils.

Acknowledgments

This study was financed in part by the Coordenação de Aperfeiçoamento de Pessoal de Nível Superior – Brasil (CAPES) – Finance Code 001, by the grant 2016/05282-2 from Fundação de Amparo à Pesquisa do Estado de São Paulo, Brasil. H. Natal da Luz acknowledges support from GAČR grant GA21-21801S (Czech Science Foundation).

References

[1] A. Cardini, G. Bencivenni, P. De Simone, The Operational Experience of the Triple-GEM Detectors of the LHCb Muon System: Summary of 2 Years of Data Taking, Tech. Rep. LHCb-PROC-2012-060. CERN-LHCb-PROC-2012-060, CERN, Geneva (Nov 2012).

[2] C. Altunbas et al., Construction, test and commissioning of the triple-GEM tracking detector for COMPASS, Nucl. Instr. Meth. A 490 (2002) 177.

[3] Upgrade of the ALICE Time Projection Chamber, Tech. Rep. CERN-LHCC-2013-020. ALICE-TDR-016 (Oct 2013).

[4] A. Colaleo, A. Safonov, A. Sharma, M. Tytgat, CMS Technical Design Report for the Muon Endcap GEM Upgrade, Tech. Rep. CERN-LHCC-2015-012. CMS-TDR-013 (Jun 2015).

[5] A. Zielińska, W. Dąbrowski, T. Fiutowski, B. Mindur, P. Wiącek, P. Wróbel, X-ray fluorescence imaging system for fast mapping of pigment distributions in cultural heritage paintings, JINST 8 (10) (2013) P10011–P10011. doi:10.1088/1748-0221/8/10/p10011.
URL https://doi.org/10.1088/1748-0221/8/10/p10011

[6] A. L. M. Silva, M. L. Carvalho, K. Janssens, J. F. C. A. Veloso, A large area full-field EDXRF imaging system based on a THCOBRA gaseous detector, J. Anal. At. Spectrom. 30 (2015) 343–352. doi:10.1039/C4JA00301B.
URL http://dx.doi.org/10.1039/C4JA00301B

[7] L. Carramate, A. Silva, C. Azevedo, S. De Francesco, A. da Silva, J. Veloso, Multi-slice energy resolving ct system using a thcobra detector operating in nech4, Nucl. Instr. Meth. A 947 (2019) 162738. doi:https://doi.org/10.1016/j.nima.2019.162738.
URL http://www.sciencedirect.com/science/article/pii/S0168900219312008

[8] H. Schindler, Garfield++ simulation of tracking detectors — user guide, https://garfieldpp.web.cern.ch/garfieldpp/, access in: 12-11-2020 (2017.2).

[9] G. G. de Souza, H. N. da Luz, XRF element localization with a triple GEM detector using resistive charge division, Nucl. Instr. Meth. A 937 (2019) 141 – 147. doi:https://doi.org/10.1016/j.nima.2019.05.058.
URL http://www.sciencedirect.com/science/article/pii/S0168900219307144

[10] B. Henke, E. Gullikson, J. Davis, X-ray interactions: photoabsorption, scattering, transmission, and reflection at E=50-30000 eV, Z=1-92, Atomic Data and Nuclear Data Tables 54 (2) (1993) 181–342.

[11] I. Smirnov, Modeling of ionization produced by fast charged particles in gases, Nucl. Instr. Meth. A 554 (1) (2005) 474 – 493. doi:https://doi.org/10.1016/j.nima.2005.08.064.
URL http://www.sciencedirect.com/science/article/pii/S0168900205016724

[12] W. R. Leo, Techniques for nuclear and particle physics experiments: a how-to approach; 2nd ed., Springer, Berlin, 1994.
URL https://cds.cern.ch/record/302344

[13] M. Ribeirete, A. Policarpo, M. Salete, S. Leite, M. Alves, E. D. Lima, Fano factors of krypton-xenon mixtures, Nucl. Instr. and Meth. 214 (2) (1983) 561 – 563. doi:https://doi.org/10.1016/0167-5087(83)90636-1.
URL http://www.sciencedirect.com/science/article/pii/0167508783906361

[14] M. Kase, T. Akioka, H. Mamyoda, J. Kikuchi, T. Doke, Fano factor in pure argon, Nucl. Instr. Meth. A 227 (2) (1984) 311 – 317. doi:https://doi.org/10.1016/0168-9002(84)90139-6.
URL http://www.sciencedirect.com/science/article/pii/0168900284901396

[15] A. Orthen, H. Wagner, H. Besch, S. Martoiu, R. Menk, A. Walenta, U. Werthenbach, Gas gain and signal length measurements with a triple-GEM at different pressures of Ar-, Kr- and Xe-based gas mixtures, Nucl. Instr. Meth. A 512 (3) (2003) 476 – 487. doi:https://doi.org/10.1016/S0168-9002(03)02053-9.
URL http://www.sciencedirect.com/science/article/pii/S0168900203020539

[16] M. J. Berger, J. H. Hubbell, S. M. Seltzer, J. Chang, J. S. Coursey, R. Sukumar, D. S. Zucker, K. Olsen, XCOM: Photon Cross Sections Database, NIST Standard Reference Database 8 (XGAM)Access in: 08-01-2021 (2010). doi:https://dx.doi.org/10.18434/T48G6X.

[17] Thompson, A. et al., X-ray Data Booklet - LBNL/PUB-490 Rev.3, Lawrence Berkeley National Laboratory, Berkeley, CA, 94720, 2009.

[18] J. Jaklevic, J. Kirby, M. Klein, A. Robertson, G. Brown, P. Eisenberger, Fluorescence detection of exafs: Sensitivity enhancement for dilute species and thin films, Solid State Communications 23 (9) (1977) 679 – 682. doi:https://doi.org/10.1016/0038-1098(77)90548-8.
URL http://www.sciencedirect.com/science/article/pii/0038109877905488

[19] L. Tröger, D. Arvanitis, K. Baberschke, H. Michaelis, U. Grimm, E. Zschech, Full correction of the self-absorption in soft-fluorescence extended x-ray-absorption fine structure, Phys. Rev. B 46 (1992) 3283–3289. doi:10.1103/PhysRevB.46.3283.
URL https://link.aps.org/doi/10.1103/PhysRevB.46.3283

[20] H. Hirayama, Lecture note on photon interactions and cross sections, kEK, High Energy Accelerator Research Organization, Tsukuba, Ibaraki, Japan, 2000.

[21] A. Kahoul, A. Abassi, B. Deghfel, M. Nekkab, K-shell fluorescence yields for elements with 6 ≤z≤ 99, Radiation Physics and Chemistry 80 (3) (2011) 369 – 377. doi:https://doi.org/10.1016/j.radphyschem.2010.11.011.
URL http://www.sciencedirect.com/science/article/pii/S0969806X10004408

[22] B. Mindur, T. Fiutowski, S. Koperny, P. Wiącek, W. Dąbrowski, Performance of a GEM detector with copper-less foils, JINST 12 (09) (2017) P09020–P09020. doi:10.1088/1748-0221/12/09/p09020.
URL https://doi.org/10.1088%2F1748-0221%2F12%2F09%2Fp09020

[23] B. Mindur, T. Fiutowski, S. Koperny, P. Wiącek, W. Dąbrowski, Investigation of Copper-Less Gas Electron Multiplier Detectors Responses to Soft X-rays, Sensors 20 (2020) 2784. doi:10.3390/s20102784.

[24] M. Chernyshova, K. Malinowski, T. Czarski, E. Kowalska-Strzęciwilk, P. Linczuk, A. Wojeński, R. D. Krawczyk, Y. Melikhov, Advantages of Al based GEM detector aimed at plasma soft-semi hard X-ray radiation imaging, Fusion Engineering and Design 146 (2019) 1039 – 1042, sI:SOFT-30. doi:https://doi.org/10.1016/j.fusengdes.2019.01.153.
URL http://www.sciencedirect.com/science/article/pii/S092037961930170X